



Cross-band infrared laser absorption of carbon monoxide for thermometry and species sensing in high-pressure rocket flows

Fabio A. Bendana¹ · Daniel D. Lee¹ · S. Alexander Schumaker² · Stephen A. Danczyk² · R. Mitchell Spearrin¹

Received: 22 August 2019 / Accepted: 27 September 2019 / Published online: 15 October 2019
© Springer-Verlag GmbH Germany, part of Springer Nature 2019

Abstract

A novel cross-band laser absorption spectroscopy technique has been developed for quantitative measurements of gas temperature and carbon monoxide (CO) in high-pressure, high-temperature rocket combustion flows. The strategy enables a broad range of sensor operability by simultaneously probing rovibrational transitions in both the fundamental and first overtone bands of CO near 4.98 μm and 2.32 μm , respectively, which sustain large differences in temperature dependence despite collisional broadening. Scanned-wavelength modulation spectroscopy methods are integrated for noise rejection in the harsh rocket operating environment. Initial experiments using the cross-band thermometry technique have been conducted on a single-element-injector rocket combustor with RP-2/GOx and CH₄/GOx propellant combinations at pressures up to 75 bar. Measurements of the first overtone bandhead (2.32 μm) maintained adequate signal-to-noise at even higher pressures (up to 105 bar), although deviating significantly from spectral simulations. To account for collisional effects at high gas densities, empirical models for line mixing, developed via shock tube studies, were employed to enable quantitative interpretation of measured signals for temperature and CO mole fraction in the rocket combustor.

1 Introduction

For chemical rockets, combustion chamber pressure directly influences mass-specific thrust, or specific impulse, which is a critical factor to enabling higher payload mass fractions and mission capability. Higher combustion pressures increase specific impulse via two primary mechanisms: (1) high pressures suppress dissociation of major products, yielding higher combustion temperatures and characteristic velocities, and (2) higher pressure ratios between the chamber and exhaust yield a higher nozzle thrust coefficient. Due to these factors, considerable effort has been placed in maximizing combustion chamber pressure in rockets. As a point of reference, Space Exploration Technologies Corp. (SpaceX) recently announced a combustion chamber pressure record of 269 bar in the new Raptor CH₄/O₂ rocket engine, which is currently in development [1]. To assess

combustion performance and support research and development of the next generation of chemical rockets, diagnostics capable of operating in high-pressure environments on this order of magnitude are needed.

Rocket combustor performance is typically evaluated through c^* efficiency, $\eta = c^*/c_{ideal}^*$, where $c^* = p_0 A^*/\dot{m}$ and involves measurement of the chamber pressure and total propellant mass flow rate. Such measurements provide a convenient global assessment of the conversion of chemical energy to thermal energy, but, because pressure is nominally constant in a combustor, they lack any information on specific internal mechanisms that may cause low combustion performance. A more granular approach would be to measure and track the changes in gas composition and temperature along the axis of flow [2]. The spatial variation of these parameters internal to a rocket combustion chamber reflects the evolution of mixing, evaporation, and chemical kinetics that dictate overall performance. Unfortunately, the extreme thermodynamic operating conditions typical of liquid-propellant rocket combustion ($T > 3000$ K, $P > 50$ bar) and sooting propensity associated with hydrocarbon fuel-rich combustion present a challenging environment for measuring temperature and species in situ [3].

Laser absorption spectroscopy (LAS) has been utilized for quantitative in situ measurements of species and

✉ Fabio A. Bendana
fbendana@ucla.edu

¹ Department of Mechanical and Aerospace Engineering, University of California, Los Angeles (UCLA), Los Angeles, CA 90095, USA

² U.S. Air Force Research Laboratory, Edwards Air Force Base, Kern County, CA 93524, USA

temperature for a variety of harsh combustion environments, including some applications to rockets. Several works have been dedicated to LAS measurements in rocket plumes near ambient pressure [4, 5], while a limited number of in-chamber measurements at elevated pressures have also been demonstrated. Specifically, Locke et al. conducted near-infrared absorption measurements of water vapor in a GH_2/GOx rocket combustor up to 8 bar [6], and Zeng et al. performed infrared absorption measurements of N_2O , NO , and CO in an ammonium-dinitramide-based rocket thrust chamber near 7 bar [7]. It can be noted that these pressures (< 10 bar) are quite low by rocket standards. At high pressures (> 50 bar), collisional broadening and blending of the spectra significantly reduce the number of isolated features for conducting thermometry and species measurements, as seen in Fig. 1, presenting unique challenges for sensor design. Recently, our research group utilized a wavelength modulation spectroscopy technique in the mid-infrared to measure CO mole fraction in a kerosene-fueled liquid rocket combustor at pressures up to 70 bar, marking a breakthrough in relevant pressure capability [8, 9]. Here, we build on this prior work, introducing a novel multi-wavelength strategy that adds in situ temperature measurement capability at practical rocket combustion pressures.

This paper describes the development and deployment of a unique cross-band infrared laser absorption spectroscopy (LAS) sensing strategy for in situ temperature and species measurements in high-pressure rocket flows. Key elements of novelty and significance include: (1) wavelength selection strategy, (2) high-pressure range capability, and (3) application to a relevant rocket combustion environment. The measurement technique simultaneously probes transitions in both the fundamental ($4.98 \mu\text{m}$) and first overtone ($2.32 \mu\text{m}$) infrared bands of nascent carbon monoxide (CO), indicated in Fig. 1, exploiting the distinct temperature dependencies at disparate

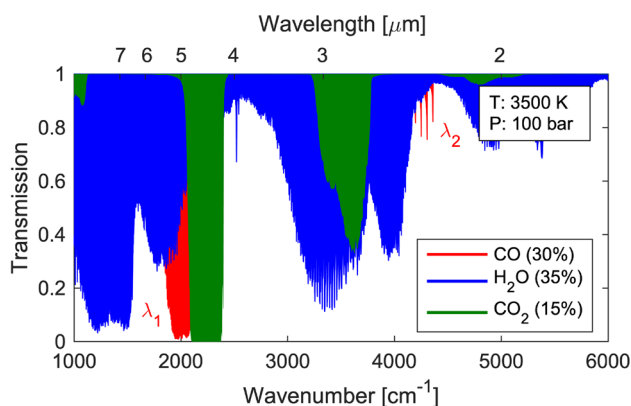


Fig. 1 Spectral transmission of CO , H_2O , and CO_2 , highlighting targeted wavelengths for the cross-band sensing strategy. Simulated conditions are representative of a liquid-propellant rocket combustor with an optical pathlength of 2.5 cm

wavelengths to achieve a broad range of sensor operability (at high pressures). Notably, deviations in spectral behavior (i.e., line mixing) at the high gas densities targeted in this work are shown to require changes in spectroscopic modeling methods to enable quantitative data interpretation. To demonstrate capability, the cross-band thermometry and species sensing method is deployed on a single-element-injector rocket combustor operating on $\text{RP-2}/\text{GOx}$ and CH_4/GOx propellant combinations, reaching pressures up to 105 bar.

2 Theory

2.1 Laser absorption spectroscopy

The theory of laser absorption spectroscopy has been discussed extensively in previous works [3, 10] and is only briefly outlined to introduce nomenclature and describe the analytical approach. For a monochromatic light source at frequency ν , the spectral absorbance α_ν through a gas medium is given by the Beer–Lambert law in Eq. (1):

$$\alpha_\nu = -\ln\left(\frac{I_t}{I_0}\right)_\nu = \sum_J S_J(T)\phi_J(\nu)NL \quad (1)$$

where I_t and I_0 are the transmitted and incident light intensities, respectively. The spectral absorbance is directly related to thermophysical gas properties as given in Eq. (1), where $S_J(T) [\text{cm}^{-1}/(\text{molec} \cdot \text{cm}^{-2})]$ is the line strength of the quantum transition J , $\phi_J(\nu) [\text{cm}]$ is the line shape function, $N [\text{molec} \cdot \text{cm}^{-3}]$ is the total number density, and $L [\text{cm}]$ is the optical pathlength.

The spectral line shape can usually be well represented by accounting for both Doppler and collisional broadening with a Voigt profile. Temperature and pressure line shape dependencies are captured within each broadening mechanism and are often characterized by the full width at half maximum (FWHM). $\Delta\nu_C [\text{cm}^{-1}]$ represents linewidth contributions due to collisional broadening and $\Delta\nu_D [\text{cm}^{-1}]$ for Doppler broadening. At the high pressures associated with rocket combustion flows, collisional broadening has a pronounced effect, typically leading to an undesirable blending of the spectra. Additionally, the blending of neighboring transitions increases the likelihood of spectral interference from other species and reduces differential absorption. The pressure dependence of $\Delta\nu_C$ is expressed in Eq. (2):

$$\Delta\nu_C = P \sum_B X_B^2 \gamma_{A-B}(T) \quad (2)$$

where P [atm] is pressure, X_B is the mole fraction of the perturbing molecule B , and $\gamma_{A-B} [\text{cm}^{-1} \text{atm}^{-1}]$ is the transition-dependent collisional broadening coefficient of the

absorbing molecule A with the perturber B . The temperature dependence of γ_{A-B} is typically captured by the power law:

$$\gamma_{A-B}(T) = \gamma_{A-B}(T_0) \left(\frac{T_0}{T} \right)^n \tag{3}$$

where T_0 [K] is a reference temperature and n is the species- and transition-specific temperature exponent. In order to minimize the unfavorable effects of line broadening and maximize pressure range capabilities, a molecule with a low collisional broadening coefficient is beneficial. The molecular dependence of collisional broadening coefficient can be expressed as: $\gamma \sim \sigma_{AB}^2 / \sqrt{\mu_{AB}}$ where σ_{AB} is the optical collision diameter and μ_{AB} the reduced mass. Therefore, targeting a molecule with a small size and large mass is favorable at high pressures.

2.2 Line mixing at high gas densities

While the previously described framework for additive line-by-line spectral absorbance modeling is adequate over a broad range of conditions, it fails to capture some collision physics at very high gas densities relevant to this work, namely line mixing. Line mixing refers to collision-induced rotational energy transfers (typically within the same vibrational levels) that distort molecular spectra at high collision frequencies. Intensity transfers between neighboring transitions are more pronounced in spectrally dense regions, such as bandheads, where line spacing is small and result in a vibrational band narrowing effect.

To model line-mixing effects at high pressures, we implement a relaxation matrix formalism [11] to capture collisional transfer rates between rotational energy levels. A rigorous theoretical discussion with modeling process details can be found in another paper from our group [12], while these steps are truncated here for brevity. It should be noted that Eq. (1) requires modification to capture spectral intensity and shape for a group of transitions encountering line mixing. For neighboring transitions, absorbance can alternatively be expressed within the impact approximation as [13, 14]:

$$\begin{aligned} \alpha_\nu &= \frac{8\pi^2}{3hc} \nu \left[1 - \exp\left(-\frac{hc\nu}{k_B T}\right) \right] L \\ &\times \sum_J \sum_K N_J d_J d_K \\ &\times \text{Im}\{\langle\langle J | [\Sigma - L_0 - iPW]^{-1} | K \rangle\rangle\} \end{aligned} \tag{4}$$

where h [J · s] is Planck’s constant, c [cm/s] is the speed of light, k_B [J/K] is the Boltzmann constant, N_J [molec · cm⁻³] is the number density of the initial level, and d_J and d_K are the weighted transition-moments. Σ [cm⁻¹], L_0 [cm⁻¹], and \mathbf{W} [cm⁻¹/atm] are operators in Liouville line space. Σ and

L_0 are diagonals associated with the wavenumber of the calculation ν and the transition line center ν_0 , respectively.

All collisional influences on spectral shape are contained in the relaxation matrix \mathbf{W} . The real diagonal elements of \mathbf{W} are the broadening coefficients γ_j discussed in Sect. 2.1, and the imaginary diagonal elements are the pressure shifts $\Delta\nu_{0,j}$ [cm⁻¹/atm]. The real off-diagonal elements represent the state-specific population transfer rates $R_{J \rightarrow K}$ [cm⁻¹/atm] from initial rotational energy level J to the final rotational energy level K . The real part of the relaxation matrix \mathbf{W} is given by:

$$\text{Re}(\mathbf{W}) = \begin{bmatrix} \gamma_1 & -R_{1 \rightarrow 2} & \dots & -R_{1 \rightarrow K} \\ -R_{2 \rightarrow 1} & \gamma_2 & \dots & -R_{2 \rightarrow K} \\ \vdots & \vdots & \ddots & \vdots \\ -R_{J \rightarrow 1} & -R_{J \rightarrow 2} & \dots & \gamma_J \end{bmatrix} \tag{5}$$

Notably, if the population transfer rates are set to zero for all transitions, Eq. (4) simply represents the sum of the Lorentzian lines with no line-mixing effects. For linear molecules, the broadening coefficient can also be written in terms of the total depopulation rates, as shown in Eq. (6) [15]:

$$\gamma_J = \sum_{J \neq K} R_{J \rightarrow K} \tag{6}$$

The imaginary off-diagonal components of \mathbf{W} represent rotational dephasing; however, previous works have found this contribution to be negligible for collisionally-narrowed infrared spectra at both low and high gas densities [16]. Accordingly, rotational dephasing contributions were approximated as zero for all transitions considered in this work. When multiple collision partners are present, the full relaxation matrix can be written as a summation of individual perturber contributions, similar to broadening.

In this study, the collision-induced population transfer rates $R_{J \rightarrow K}$ were modeled using a modified-exponential-gap (MEG) law, as shown in Eq. (7):

$$\begin{aligned} R_{J \rightarrow K} &= a_1(T) \left[\frac{1 + a_4 \left(\frac{E''_J}{a_2 k_B T} \right)}{1 + a_4 \left(\frac{E''_K}{k_B T} \right)} \right]^2 \\ &\times \exp \left[\frac{-a_3 (E''_K - E''_J)}{k_B T} \right] \end{aligned} \tag{7}$$

where E'' [cm⁻¹] is the lower state energy and $a_1(T)$ [cm⁻¹/atm], a_2 , and a_3 are species-specific MEG law coefficients. a_4 describes the collision duration [17] based on distance of closest approach [18]. The temperature dependence of $a_1(T)$ can be modeled using a power law analogous to the broadening coefficient. The MEG law coefficients used in this work were obtained from previous line-mixing

studies conducted by our research group [12]. Since collisions promote the Boltzmann population distribution, the upward and downward population transfer rates can be related through the detailed-balance principle [19]:

$$\rho_K R_{K \rightarrow J} = \rho_J R_{J \rightarrow K} \quad (8)$$

where ρ is defined as the Boltzmann population fraction. The detailed-balance principle suggests that line mixing favors population transfers from weak transitions to strong transitions, inducing a spectral band narrowing effect and enhancing high-absorbing regions. Consequently, narrowing of the spectral shape due to line mixing preserves differential absorption at high pressures and has potential to extend pressure capabilities of scanned-wavelength laser absorption methods.

2.3 Scanned-wavelength modulation spectroscopy

A scanned-wavelength modulation spectroscopy (WMS) technique with second harmonic ($2f$) normalized detection was implemented for all laser absorption measurements conducted in this work. Scanned-WMS has proven advantageous for sensing applications in harsh environments because of its insensitivity to noise in the transmitted light intensity, which may result from mechanical vibrations of the test article, window fouling, dynamic thermal emission, or particle scattering. The technique is well detailed in literature [20, 21] but is briefly reviewed for context.

Measurements are conducted by rapidly injection-current tuning the laser with a high-frequency sinusoidal waveform superimposed on a low-frequency sinusoidal waveform to modulate laser intensity and wavelength over the target absorption feature. The optical output frequency of the laser $\nu(t)$ can be modeled through Eq. (9):

$$\begin{aligned} \nu(t) &= \bar{\nu}_L + \nu_S(t) + \nu_M(t) \\ &= a_S \sin(f_S t + \psi_S) + a_M \sin(f_M t + \psi_M) \end{aligned} \quad (9)$$

where $\bar{\nu}_L$ is the center frequency of the modulation, ν_S is the scan frequency, and ν_M is the modulation frequency. The subscripts S and M denote the scan and modulation, respectively, where a_S is the scan depth, a_M is the modulation depth, f is the frequency, and ψ is the corresponding phase shifts. These parameters are predetermined in the laboratory subject to laser tuning characteristics (as discussed in Sect. 3.2), as they directly influence the harmonic signal strength and the signal-to-noise ratio (SNR) of the measurement. The harmonics of the wavelength modulation are related to the absorbance spectra and can be simulated using the approach of Sun et al. [22]. The raw detector signal is post-processed through a lock-in amplifier to isolate the harmonic signals of the modulation frequency and eliminate noise outside the prescribed passband. The second harmonic signal is sensitive to the absorption line shape curvature

(differential absorption) and can be compared to a spectral model to infer gas properties. Non-absorbing transmission losses and noise in the transmitted light intensity are negated by normalizing the second harmonic WMS signal ($2f$) by the first harmonic ($1f$). The $1f$ normalized-WMS $2f$ technique is well suited to the harsh rocket engine environment that involves dynamic non-absorption-related light intensity distortion.

3 Sensor design

3.1 Wavelength selection

Rocket combustors typically operate fuel-rich and at relatively extreme thermodynamic conditions ($P > 50$ bar, $T > 3000$ K). For a hydrocarbon fuel and oxygen, the equilibrium combustion product mixture includes a large fraction (%) of infrared-active diatomic species (OH, CO) as well as the major products (CO_2 , H_2O). High concentrations of carbon monoxide ($X_{\text{CO}} > 30\%$) provide an attractive target to track changes in gas composition and thermodynamic state as a measure of combustion progress. CO has smaller collisional cross sections than the larger polyatomic products (e.g., CO_2 , H_2O) and therefore can have substantially less spectral broadening at high pressures, as discussed in Sect. 2.1 [10]. This fundamental spectroscopic characteristic helps preserve differential absorption and lessens interference at elevated pressures, providing a basis for the development of an LAS thermometry technique above the pressure

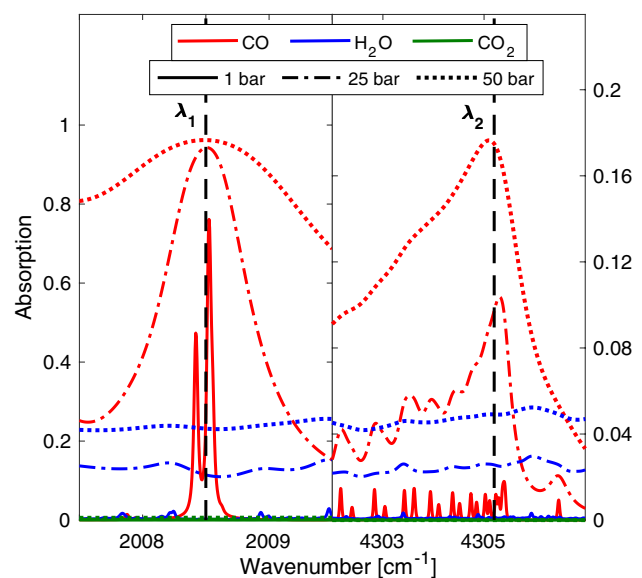


Fig. 2 Simulated absorption spectra in CO's fundamental band and first overtone band, illustrating collisional effects at high pressures. Simulated conditions: $T = 3500$ K, $X_{\text{CO}} = 30\%$, $X_{\text{H}_2\text{O}} = 30\%$, $X_{\text{CO}_2} = 10\%$

limits (~ 50 bar) of previous work [23]. Accordingly, this effort targets carbon monoxide absorption in the infrared.

Gas temperature and species mole fraction are commonly inferred using a two-wavelength absorption technique [10]. Wavelength-pair selection criteria include: (1) absorbance between optically thin and thick limits, (2) minimal interference from other absorbing species, and (3) high temperature sensitivity. All three of these criteria become more challenging to meet at high gas pressures. As aforementioned, collisional broadening scales linearly with pressure and blends transitions. This reduces differential absorbance and increases interference. Moreover, due to scaling of absorbance with gas density, the stronger vibrational bands can become optically thick at relatively short pathlengths in high-pressure environments. Figure 1 highlights these issues, showing simulated transmission through a 2.5 cm optical path for a representative hydrocarbon rocket combustion product mixture at 100 bar. Due to extreme line broadening, spectral interference by H_2O and CO_2 is prevalent throughout the infrared. The CO spectra (shown in red) can be accessed in the P-branch of the fundamental band near $4.98\ \mu\text{m}$ and in the R-branch bandheads of the first overtone near $2.32\ \mu\text{m}$, with minimal but not entirely avoidable interference. Zoomed-in regions of this domain can be seen in Fig. 2. The wavelength region near $4.98\ \mu\text{m}$ is dominated by the P($J = 31$) line of the ground state fundamental band, but also includes contributions from other neighboring hot band lines [8]. The first overtone bandhead near $2.32\ \mu\text{m}$ consists of multiple transitions ($J = 40\text{--}60$) belonging to the $\nu(1 \rightarrow 3)$ hot band, with some overlapping contributions from the ground state $\nu(0 \rightarrow 2)$ first overtone band [12].

For thermometry, ideally two neighboring lines or wavelengths can be accessed with a single light source and/or

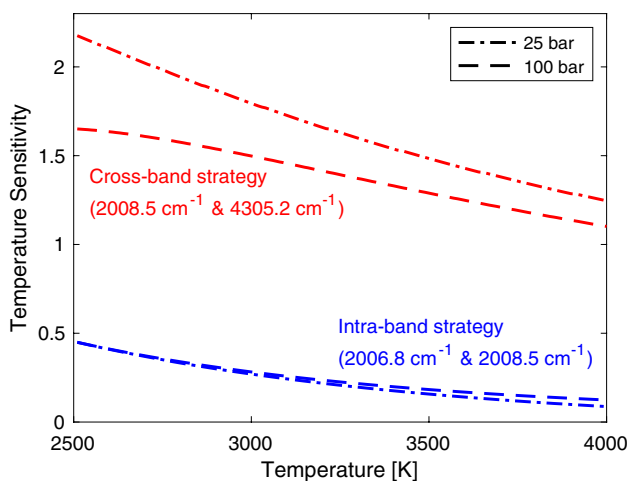


Fig. 3 Temperature sensitivity ($dR/R)/(dT/T)$ of the cross-band sensing strategy compared to more traditional intra-band sensing strategies at elevated pressures

shared detection optics. Unfortunately, at very high pressures the local spectra within a band becomes sufficiently blended that wavelengths in close proximity have increasingly similar temperature dependence, determined by the aggregate line strengths and lower state energy levels of the many overlapping transitions. This results in accessible wavelength pairs within the same band having poor temperature sensitivity, which reduces thermometry range and accuracy. This effect is quantified and shown in Fig. 3. A candidate intra-band wavelength pair was selected within the accessible low-interference region of the fundamental band near $4.98\ \mu\text{m}$. However, the temperature sensitivity of the local peak absorbance ratio, $R = \alpha(\lambda_1)/\alpha(\lambda_2)$, was found to be undesirably low. To resolve this limitation, a cross-band wavelength pair from the disparate fundamental (λ_1 : $4.98\ \mu\text{m}$) and first overtone (λ_2 : $2.32\ \mu\text{m}$) bands of carbon monoxide was considered and proved to yield superior temperature sensitivity at high pressures, consistent with other cross-band techniques [24–26]. The specific wavelength selections are shown in Fig. 2.

Spectral interference from other major infrared-active hydrocarbon combustion products is minimal at both wavelengths relative to the surrounding domain, but significant on an absolute basis. A scanned-wavelength modulation spectroscopy technique employing normalized second harmonic detection is utilized to recover signals related to the differential absorption at each wavelength in the harsh rocket environment, similar to our prior work [8]. This approach generally negates the influence of baseline signal changes including attenuation associated with spectrally-flat absorption such as the H_2O interference noted in Fig. 2 [20, 22].

3.2 Optimizing laser tuning parameters

As mentioned, the scan and modulation depths (a_S and a_M) and associated tuning frequencies (f_S and f_M) of the optical output can be adjusted to optimize the quality of the WMS harmonic signals for a target gas condition and measurement environment. A model of the WMS harmonics based on laser-specific tuning characteristics is utilized to inform parametric optimization [22]. For this sensor, optimum modulation depth is deemed the value at which the WMS- $2f$ signal is maximized. Although the $2f$ and $1f$ signals are typically not maximized at the same modulation depth, maximizing $2f$ generally increases the signal-to-noise of the normalized WMS- $2f/1f$ measurement. In probing high-pressure spectra, rapidly tunable semiconductor lasers are often unable to achieve an optimal modulation depth and the $2f$ monotonically increases with a_M until it reaches a maximum limit. SNR can be further influenced by modulation frequency. Modulating at higher frequencies enables high time resolution measurements and typically suppresses noise. Common noise sources (vibrations, beam steering,

etc.) in engine applications usually occur at relatively low frequencies (< 10 kHz) and can be mitigated by modulating at much higher frequencies and filtering around those frequencies. Unfortunately, modulation frequency has an inverse relationship with modulation depth (see Fig. 4 (top)), and thus, a compromise is required between the competing demands of signal quality and time resolution. Additionally, adding a low-frequency waveform to the high-frequency modulation further reduces the maximum modulation depth available. The low-frequency scan is added to ensure that the local absorption peak is measured, allowing for some uncertainty in the pressure shift of the targeted transitions. However, since it is not necessary to fully resolve the harmonic spectra to interpret measurement data, the scan depth of the low-frequency waveform can be minimized in order to maximize the modulation depth.

Figure 4 (top) illustrates the maximum modulation depth at different frequencies for the two lasers chosen for the cross-band technique. To target CO's fundamental band near $4.98 \mu\text{m}$ and first overtone band near $2.32 \mu\text{m}$, a distributed feedback (DFB) quantum cascade laser (QCL) and DFB diode laser are utilized, respectively. The maximum modulation depth is determined by injecting the maximum allowable current range at a given frequency and measuring the corresponding change in relative wavenumber with a germanium etalon. For both light sources, maximum modulation depth is shown to decrease logarithmically as frequency increases. Figure 4 (bottom) also illustrates the simulated WMS- $2f$ signals ($a_M = 0.5 \text{ cm}^{-1}$) for both lasers

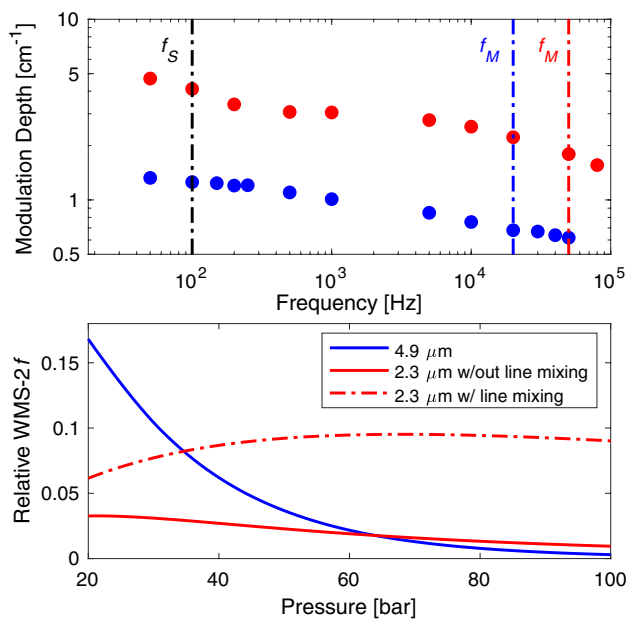


Fig. 4 (top) Maximum modulation depth over a range of frequencies for the QCL near $4.98 \mu\text{m}$ and the DFB diode near $2.32 \mu\text{m}$. (bottom) Simulated WMS- $2f$ signals ($a_M = 0.5 \text{ cm}^{-1}$) over a range of pressures

over a range of pressures at the targeted wavelengths for a representative rocket combustion condition. As pressure increases and the spectra broadens, the second harmonic signal generally decreases due to its sensitivity to line shape curvature, which is diminishing. As a result, it is desired to utilize a large modulation depth at high pressures to fully capture the spectral shape and maximize pressure range capability. When comparing the two wavelengths, the WMS- $2f$ from the fundamental band starts higher but decreases at a much faster rate than the overtone band. This relates to the favorable characteristics of the bandhead in retaining spectral structure at extreme conditions. Furthermore, the bandhead region is subject to high-pressure line-mixing effects, which induce a spectral narrowing of the vibrational band and preserves differential absorption. Consequently, accounting for line mixing results in a higher WMS- $2f$ signal across all pressures in the first overtone band. The benefit of exploiting this phenomenon increases with increasing pressure. Figure 4 (bottom) shows that at 100 bar, line mixing results in nearly an order of magnitude gain in the WMS- $2f$ signal relative to the simulation that ignores line mixing (discussed further later).

For the present work, a scan depth of 0.13 cm^{-1} at 100 Hz was chosen for the QCL near $4.98 \mu\text{m}$. The remaining injection-current budget was allocated to a modulation depth of 0.50 cm^{-1} at 20 kHz. For the DFB diode laser centered near $2.32 \mu\text{m}$, a scan depth of 2.55 cm^{-1} at 100 Hz was utilized. Similar to the QCL, the remaining injection-current budget was devoted to a modulation depth of 0.48 cm^{-1} at 50 kHz. These parameters were selected as a compromise of the competing demands aforementioned, aiming to achieve high WMS- $2f$ signal quality (SNR) over a pressure range of 20–100 bar.

3.3 Optical interface

Figure 5 illustrates the optical configuration for the cross-band absorption sensing technique and hardware interface for conducting measurements at a fixed axial location on the target liquid bipropellant rocket combustor. To probe the fundamental CO absorption band near $4.98 \mu\text{m}$ and the first overtone band near $2.32 \mu\text{m}$, a DFB QCL with $\sim 50 \text{ mW}$ output power and a DFB diode laser with $\sim 5 \text{ mW}$ output power are utilized, respectively. An inherent challenge presented by this approach is the wavelength-specific nature of many optical components (e.g., detectors, fibers) that potentially increases sensor complexity. To reconcile this, both incident beams are free-space coupled into one hollow-core fiber with broad transmissivity ($300 \mu\text{m}$ diameter) [27, 28]. The fiber output is then re-collimated using another CaF_2 lens and is transmitted across the combustion chamber through two wedged sapphire windows ($3/8$ in. diameter with 1° wedge). The sapphire

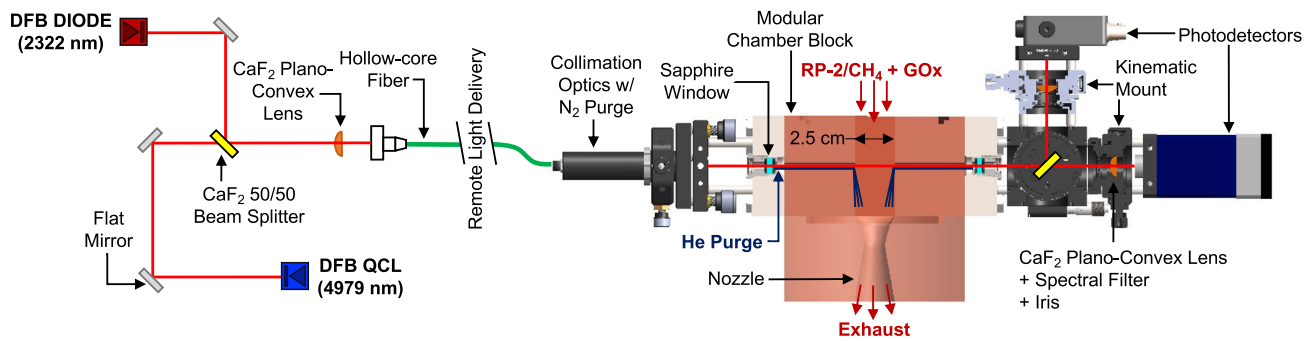


Fig. 5 Optical interface for high-pressure CO sensing measurements in a liquid-propellant rocket combustor. Notable features include a hollow-core fiber for remote light delivery and a He/N₂ purge system to maintain clear optical access

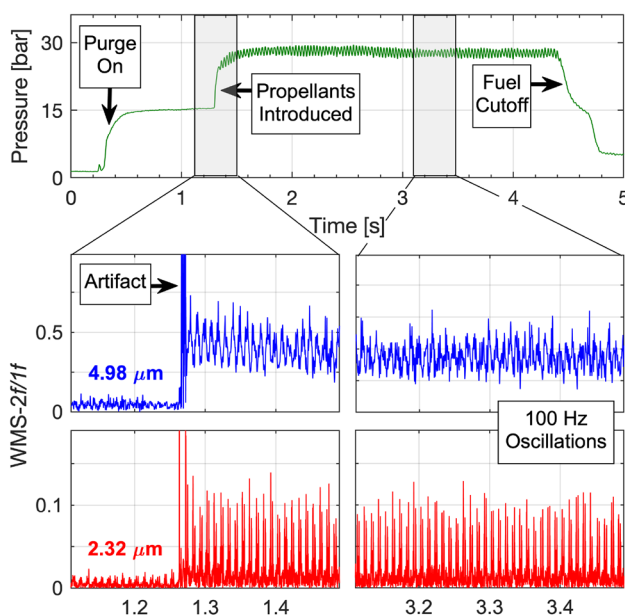


Fig. 6 Time evolution of chamber pressure and corresponding WMS- $2f/1f$ signals (background subtracted) for 4.98 μm and 2.32 μm

windows have an aperture of 4 mm and are recessed ~ 5 cm from the combustion flow path. A beam splitter separates the transmitted light so that each beam can be spectrally filtered for its respective wavelength (Spectrogon, 2320 ± 20 nm and 4960 ± 148 nm) before being collected on distinct thermoelectrically cooled photodetectors. An InGaAs photodetector (Thorlabs PDA10D) with 15 MHz bandwidth is utilized for 2.32 μm light and a MCT photovoltaic detector (Vigo PVI-4TE-5-1) with 10 MHz bandwidth is utilized for 4.98 μm light. Measurements are taken across a 2.5 cm transverse optical pathlength located ~ 32 cm downstream of the single-element injector. Raw detector data were typically collected at a sample

rate of 10 MHz for 5-s intervals with hot-fires spanning 2–3 s in duration.

The optical setup described above included mechanical mounts for beam pointing and translation, which were used to optimize alignment and maximize the transmitted light intensity during the experiment. A number of complementary hardware-related elements, including a N₂ purge system in the fiber-optic and pitch assembly and a He purge system in the chamber, were implemented to mitigate signal-convoluting factors in the test environment. The N₂ purge system displaces excessive water vapor in the optical path that can spectrally interfere with CO. The He purge system aims to minimize soot deposition on the sapphire windows by keeping the optical path clear [29]. Laser tuning and signal processing methods discussed in Sect. 2.3 were also chosen to mitigate environmental noise.

4 Experimental results

4.1 Initial sensor demonstration

A series of measurements over a range of pressures and mixture ratios (MR) were conducted on a single-element-injector rocket combustor with both CH₄/GOx and RP-2/GOx as propellants. The test facility is located at the Air Force Research Laboratory on Edwards Air Force Base. These measurements build on prior research from our group conducted at the same facility by introducing the cross-band thermometry that enables in situ temperature measurement capability at practical rocket combustion pressures [8]. For the tests discussed here, the modular chamber block with optical access was located at the furthest location downstream of the injector (~ 32 cm), where complete combustion and mixing is most likely to occur. Measurements using CH₄/GOx were conducted at

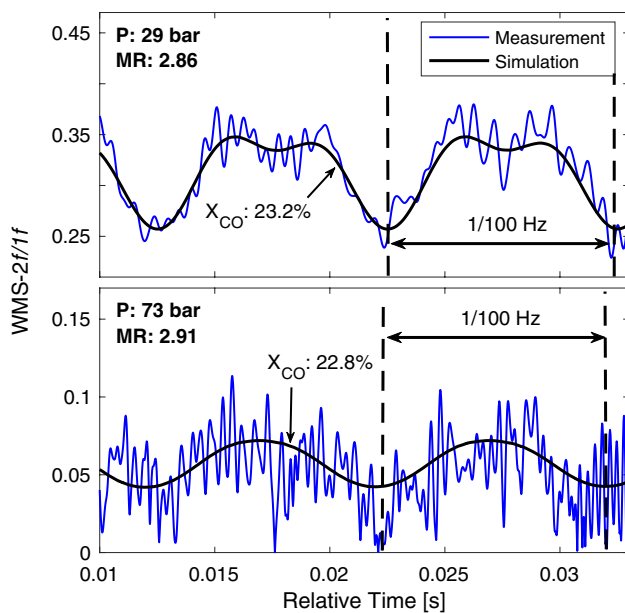


Fig. 7 Measured WMS- $2f/1f$ signals near $4.98\ \mu\text{m}$ compared to a chemical equilibrium simulation at two chamber pressures and mixture ratios

pressures and MR ranging from 25 to 105 bar and 2.2 to 4, respectively, while pressures and MR using RP-2/GOx ranged from 25 to 75 bar and 2.5 to 4.5, respectively. The details discussed below focus on experiments using CH_4/GOx as propellants but are generally representative of all datasets.

Raw optical signals at both wavelengths were processed through a digital lock-in amplifier to extract the WMS harmonics, from which gas properties could be interpreted. Figure 6 shows the pressure evolution in time for an example test with corresponding WMS- $2f/1f$ signals at $4.98\ \mu\text{m}$ and $2.32\ \mu\text{m}$ for a steady-state chamber condition of 28 bar and MR of 2.33. The WMS- $2f/1f$ signals are background subtracted, with the background taken prior to ignition. The initial rise in pressure around 0.3 s is associated with the purge gas. An abrupt increase in both the pressure and WMS- $2f/1f$ signals around 1.3 s corresponds to the introduction of propellants and ignition, indicating CO presence in the combustor. As chamber pressure increases toward steady state, the WMS- $2f/1f$ signals slightly decrease due to spectral broadening and reduced differential absorption (more pronounced in the $4.98\ \mu\text{m}$ signal). At steady state, 100 Hz oscillations, corresponding to the scan frequency of each laser, become clearly evident in both the $4.98\ \mu\text{m}$ and $2.32\ \mu\text{m}$ signals. As mentioned in Sect. 3.3, hot-fire tests typically span a 2–3 s duration with detector data sampled for 5 s.

Figures 7 and 8 compare measured WMS- $2f/1f$ signals to WMS- $2f/1f$ simulations assuming chemical equilibrium

for mixture composition and temperature and the HITEMP database [30] for spectral parameters for both $4.98\ \mu\text{m}$ and $2.32\ \mu\text{m}$. The WMS harmonics are extracted by using a digital lock-in amplifier and a 2 kHz passband filter and then averaged over ~ 50 cycles throughout the steady-state chamber condition. Figure 7 illustrates the measurement at the fundamental band for two conditions: 29 bar with a MR of 2.86 and 73 bar with a MR of 2.91. The 100 Hz oscillations from the laser scan (present in Fig. 6) are more clearly evident in these zoomed-in WMS- $2f/1f$ signals. The measurements conducted near $4.98\ \mu\text{m}$ demonstrated relatively close agreement with the simulated model at chemical equilibrium. At higher pressures, spectral broadening and reduced differential absorption lower the SNR of the fundamental band; however, a measurement is still discernible at pressures up to 75 bar, consistent with our prior work [8]. Figure 8 illustrates the measurement at the first overtone bandhead for two conditions: 28 bar with a MR of 2.33 and 105 bar with a MR of 2.93. Notably, the SNR only modestly decreases across this wide pressure range. However, the measured and simulated WMS- $2f/1f$ signals exhibit substantial disagreement, beyond typical uncertainties, in both magnitude and spectral shape, indicating a fundamental error in the spectroscopic modeling of the first overtone band. This was suspected to be a consequence of line-mixing effects (discussed in Sect. 2.2), which occur in spectrally-dense regions [31], such as the bandhead, and were unaccounted for in the original model. In Fig. 8, estimates of

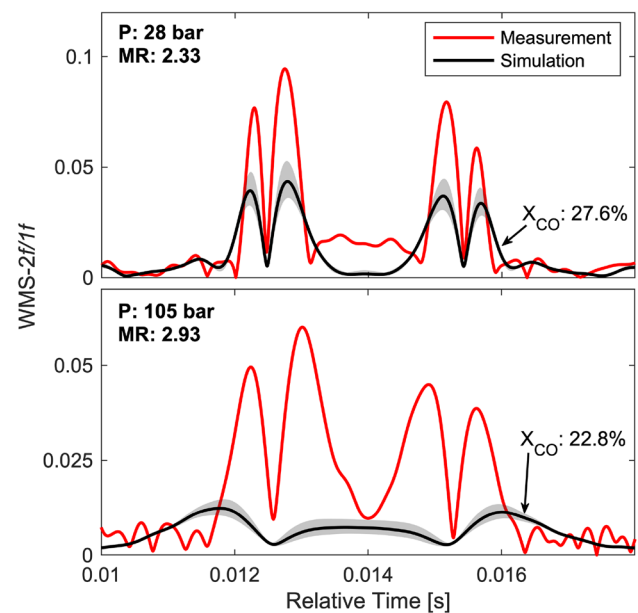


Fig. 8 Measured WMS- $2f/1f$ signals near $2.32\ \mu\text{m}$ compared to a chemical equilibrium simulation with initial estimates of spectroscopic uncertainty ($\gamma_{\text{mix}} \pm 10\%$) bound in gray at two chamber pressures and mixture ratios

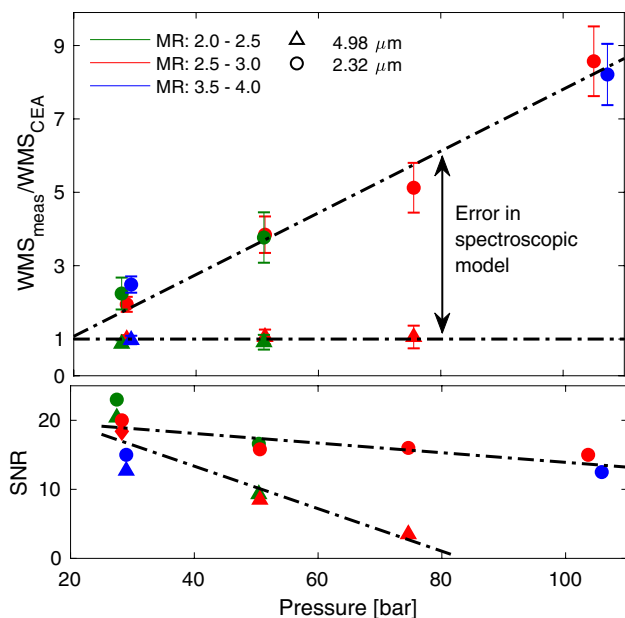


Fig. 9 Measured WMS- $2f/1f$ signals with SNR compared to chemical equilibrium simulations for both 4.98 μm and 2.32 μm over relevant mixture ratios and pressures

broadening-related error ($\gamma_{\text{mix}} \pm 10\%$) are added to the spectral simulation to elucidate the extent of the disagreement.

Similar data analysis was carried out for a series of test conditions represented in Fig. 9, which highlights trends in SNR and accuracy of the initial simulation model. Measured WMS- $2f/1f$ signals are normalized by simulated WMS- $2f/1f$ signals and plotted over the range of pressures and MR conducted. As mentioned previously, the simulated WMS- $2f/1f$ signal assumes chemical equilibrium for temperature and composition and the HITEMP database parameters with Voigt lineshapes for spectral properties. The WMS signals at 4.98 μm show good agreement with NASA’s Chemical Equilibrium with Applications (CEA) software [32] and HITEMP up to 75 bar. However, as pressure increases, collisional-broadening effects in the fundamental band cause the targeted absorption features to broaden and the differential absorption to diminish (see Fig. 2). This results in a diminishing SNR that approaches unity around 80 bar, deeming any measurements at extended pressures unreliable. The measured WMS signal at 2.32 μm demonstrated adequate signal quality (SNR > 10) at pressures up to 105 bar, as seen in Fig. 8. However, disagreement between the simulated and measured signals was substantial, increasing nearly linearly with pressure to almost an order of magnitude disagreement at the highest pressures. As discussed previously, such disagreement was deemed well beyond the typical uncertainties in the simulation and hypothesized to be a more fundamental error in the spectroscopic model assumptions. It can be noted that by assuming a temperature, the

fundamental band measurement near 4.98 μm could solely be used to infer CO concentration, as demonstrated in previous works [8, 9]. To measure temperature, both wavelengths are needed. Therefore, to reconcile the large disagreement between the simulated and measured signals near 2.32 μm , a deeper investigation of the spectral characteristics of the targeted CO $\nu(1 \rightarrow 3)$ bandhead was initiated.

4.2 Interpretation of line-mixing effects

Line-mixing effects in the $\nu(1 \rightarrow 3)$ first overtone bandhead of CO at high temperatures and high pressures have been recently studied by our research group on a high-enthalpy shock tube [12]. Direct absorption measurements of CO near 2.32 μm were conducted behind reflected shock waves over a range of pressures (5–60 bar) and temperatures (1200–3750 K) relevant to liquid-propellant rocket combustors. An example of the spectroscopic data highlighting the non-ideal phenomena and modeling at these conditions is discussed briefly here, while a more comprehensive dataset and discussion are available in another paper by the authors [12]. As seen in Fig. 10, the measured absorption spectra at a representative rocket condition demonstrate large disagreement when compared to a simulated spectra with no line-mixing effects. The translation of this disagreement to the WMS- $2f/1f$ signal can also be observed. At high gas densities, collision-induced rotational energy transfers within the same vibrational band induce a spectral narrowing

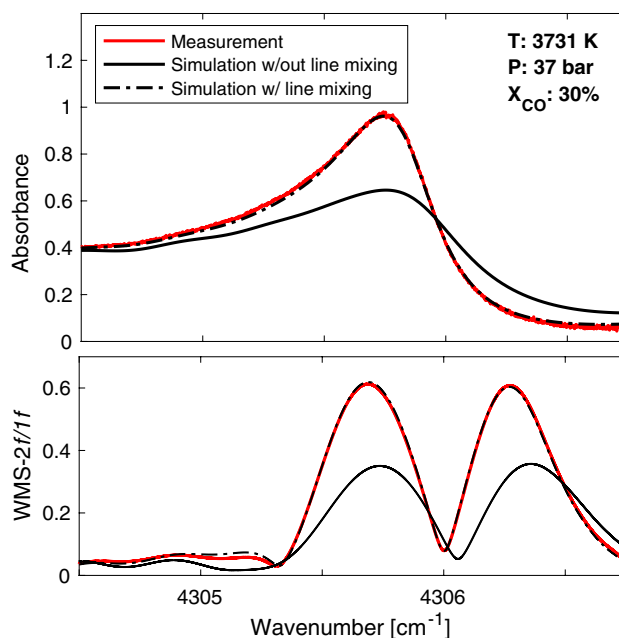


Fig. 10 CO absorbance measurement of the first overtone bandhead near 2.32 μm with corresponding WMS- $2f/1f$ signals compared to an empirical MEG law model accounting for line-mixing effects and a spectral simulation with no line mixing

effect that amplifies high-absorbing regions. This results in larger differential absorption (i.e., larger $WMS-2f / 1f$) in the measured spectra, as observed in the initial sensor demonstration in Fig. 8. In order to model the collision-induced population transfers between transitions near the bandhead, a modified-exponential gap (MEG) rate law was adopted [33–35] (discussed in Sect. 2.2). The adjustable parameters in the MEG law were obtained by implementing a least-squares fitting routine to the measured data. This allowed line-mixing effects to be accounted within the absorption modeling framework described in Sect. 2.2. Measurements over a range of pressures and temperatures further provide for scaling over the full range of relevant thermodynamic conditions present in a rocket combustion chamber. Figure 10 illustrates that the simulated spectra using the MEG law can accurately represent CO absorption in first overtone bandhead. Similarly, the updated spectroscopic line-mixing model in Fig. 10 shows the improved agreement in $WMS-2f / 1f$ signal that can be achieved by accounting for line-mixing effects.

The controlled shock tube investigation provided concrete support of the line-mixing hypothesis for the initial disagreement observed in the field data and, with appropriate estimates for the population transfer rates, provides a critical new framework for quantitative interpretation of the CH_4/GOx and RP-2/ GOx rocket combustor data. The shock tube study focused on quantifying collisional transfer rates and broadening for pure CO and CO perturbed by Ar. In order to account for species-dependent collisional broadening and line mixing in the rocket gas mixtures, additional assumptions were required. Notably, chemical equilibrium was assumed to dictate the composition for the range of

mixture ratios and pressures tested. Species-specific spectral parameters and MEG law coefficients were used where available in the literature for other perturbors [35–38], and otherwise scaled with ratios of broadening coefficients consistent with Eq. (6). The modified absorption model was integrated into the WMS harmonic simulations to interpret the high-pressure rocket combustor data.

4.3 High-pressure rocket characterization

With a modified absorption model to account for line-mixing effects at high pressures, the WMS signal from CO's first overtone band (shown in Fig. 8) can be interpreted and utilized with the fundamental band (shown in Fig. 7) to quantitatively infer temperature and CO mole fraction. Temperature is obtained by taking the ratio of the measured peak $WMS-2f / 1f$ signals from the two wavelengths and comparing to simulated values. With temperature known, CO concentration can be inferred from absolute $WMS-2f / 1f$ signal magnitude [8, 22]. Figure 11 compares measured temperatures and mole fractions to chemical equilibrium. The chemical equilibrium results are bounded by the highest and lowest pressures measured, 105 bar and 28 bar, respectively, and shown for reference. In order to obtain mole fraction measurements above 100 bar, where the SNR at $4.98 \mu m$ drops below unity, the chemical equilibrium temperature was assumed, and the first overtone bandhead ($2.32 \mu m$), which exhibited promising signal quality ($SNR > 10$) even at the highest pressures (> 100 bar), was solely used to infer mole fraction.

Representative error bars in temperature and mole fraction based on the standard deviation of the measured

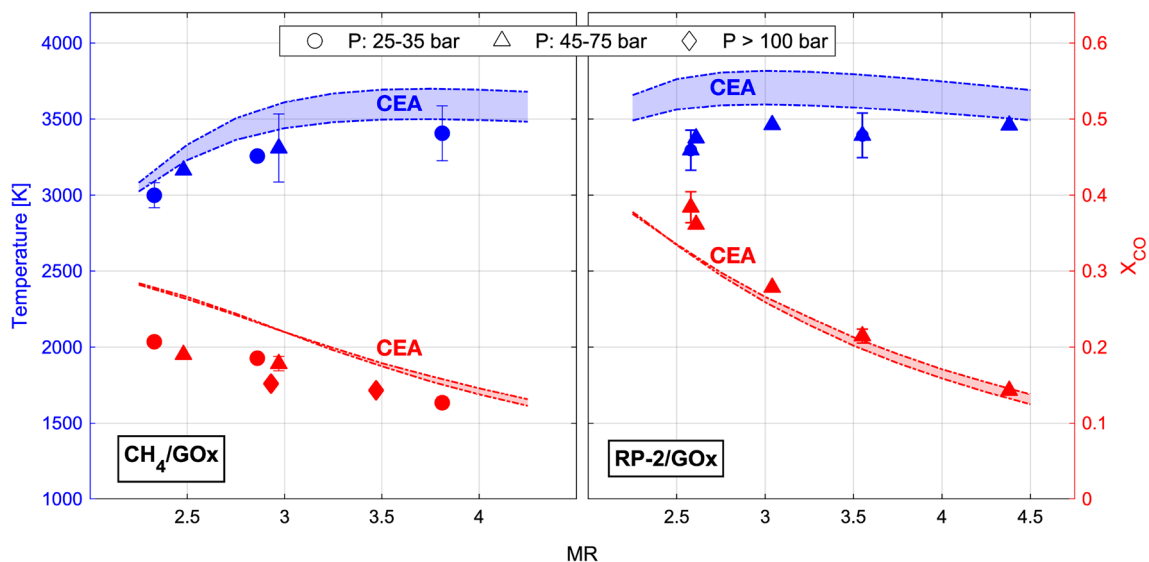


Fig. 11 Temperature and species measurements with representative error bars at steady-state combustor conditions for CH_4/GOx and RP-2/ GOx up to 105 bar. Measured temperature and mole fractions are compared to chemical equilibrium over a range of mixture ratios and pressures

harmonic signals are shown in Fig. 11. Temperature precision for all CH₄/GOx and RP-2/GOx tests ranged from 5 to 14% and 5 to 9%, respectively, while mole fraction precision ranged from 6 to 12% for both fuels. The highest potential error (worst precision) occurs at the highest pressures, as expected. The inferred temperatures from all tests followed the expected trends but were slightly lower (generally by 100–300 K) than equilibrium temperature, indicative of incomplete combustion, poor mixing, heat losses, or a cold boundary layer. For inferred CO mole fraction, more distinct differences have been observed between the two fuels. Species measurements from CH₄/GOx tests were consistently less than chemical equilibrium while measurements from RP-2/GOx testing were nearly equivalent or slightly higher. This discrepancy may be attributed to the differences in single-element injector designs and performance, suggesting lower performance with the CH₄/GOx configuration, consistent with lower *c** efficiency measured independently. It should also be noted that modest uncertainty remains in the spectroscopic model related to composition-dependent collisional broadening and line mixing. Even with these uncertainties, mole fraction measurements for both fuels follow the trend anticipated from chemical equilibrium in close proximity. The differences observed between fuel and injector combinations support the utility of the sensor in evaluating rocket combustion performance.

5 Conclusion

A novel cross-band infrared laser absorption sensing strategy probing carbon monoxide at the vibrational bands near 4.98 μm and 2.32 μm was developed and deployed to quantitatively measure temperature and species concentration in high-pressure rocket combustion environments. The initial target application for the diagnostic technique was a single-element-injector rocket combustor at the U.S. Air Force Research Laboratory, Edwards. Measurements were performed by collecting and interpreting harmonics of wavelength modulation (WMS-2*f*/1*f*) related to absorption at each target wavelength over a range of pressures and mixture ratios for both CH₄/GOx and RP-2/GOx propellant combinations. The method exhibited an ability to overcome challenges associated with the extreme thermodynamic conditions and sooting propensity of the rocket combustor. Data collected at the fundamental vibrational band (4.98 μm) showed reliable signal quality up to 75 bar, while data from the first overtone bandhead (2.32 μm) exhibited favorable SNR up to 105 bar, with the clear potential to conduct measurements at even higher pressures.

In order to interpret the signals from the first overtone bandhead, a modified spectroscopic model was developed to account for the temperature- and pressure-dependent

line-mixing effects occurring at high gas densities. Using the modified absorption model, temperatures in the rocket combustor were successfully inferred to be in the 2900–3600 K range for the various tests, showing similar but consistently lower values than equilibrium predictions by 3–12%. Quantitative characterization of temperature and species in the rocket combustion gases for the CH₄ and RP-2 fuels identified possible differences in injection/mixing performance that likely cause the disagreements with equilibrium predictions. Notably, the injector appeared to perform worse for the CH₄/GOx configuration, most pronounced by relatively low CO mole fraction values suggesting incomplete combustion. To the authors' knowledge, these measurements represent new limits in pressure capability for non-intrusive temperature and species combustion diagnostics. More importantly, the unique pressure capability of the sensing strategy provides for a useful method for evaluating combustion efficiency/performance at practical rocket operating conditions and novel datasets that can be compared to reacting flow computational models.

Acknowledgements This work was sponsored by the Air Force Research Laboratory under Award No. 16-EPA-RQ-09. The authors would like to thank Anil P. Nair for assistance in conducting CH₄/GOx experiments, Dr. William A. Hargus and Dr. John W. Bennewitz for help in setting up the data acquisition system, and Dr. Daniel I. Pineda and Chuyu Wei for ongoing support in developing the line-mixing model. The fundamental spectroscopy work is partially supported by the U.S. National Science Foundation, Award No. 1752516.

References

1. D. Paez. SpaceX's Starship Engine Shattered a Long-Standing Russian Rocket Record (2019)
2. P.G. Hill, C.R. Peterson, *Mechanics and Thermodynamics of Propulsion*, 2nd edn. (Addison-Wesley Publishing Co, Reading, MA, 1992)
3. C.S. Goldenstein, R.M. Spearrin, J.B. Jeffries, R.K. Hanson, *Prog. Energy Combust. Sci.* **60**, 132–176 (2017)
4. A.W. Caswell, S.T. Sanders, M.J. Chiaverini. Swept-wavelength laser absorption tomography for imaging rocket plume gas properties, in *41st AIAA/ASME/SAE/ASEE Joint Propulsion Conference & Exhibit* (2005)
5. A.S. Makowiecki, T.R. Hayden, M.R. Nakles, N.H. Pilgram, N.A. MacDonald, W.A. Hargus, G.B. Rieker. Wavelength modulation spectroscopy for measurements of temperature and species concentration downstream from a supersonic nozzle, in *53rd AIAA/SAE/ASEE Joint Propulsion Conference* (2017)
6. J. Locke, S. Pal, R. Woodward, R. Santoro. Diode laser absorption spectroscopy measurements in a gaseous hydrogen/oxygen rocket, in *49th AIAA Aerospace Sciences Meeting including the New Horizons Forum and Aerospace Exposition* (2011)
7. H. Zeng, F. Li, X. Yu, D. Ou, L. Chen, *Appl. Opt.* **57**, 1321–1330 (2018)
8. D.D. Lee, F.A. Bendana, S.A. Schumaker, R.M. Spearrin, *Appl. Phys. B* **124**, 77 (2018)
9. D.D. Lee, F.A. Bendana, R.M. Spearrin. Laser absorption spectroscopy of carbon monoxide near 4.97 μm for temperature and

- species measurements in hydrocarbon-fueled rockets, in *2018 AIAA Aerospace Sciences Meeting* (2018)
10. R.K. Hanson, R.M. Spearrin, C.S. Goldenstein, *Spectroscopy and Optical Diagnostics for Gases* (Springer, Berlin, 2016)
 11. U. Fano, *Phys. Rev.* **131**, 259–268 (1963)
 12. F.A. Bendana, D.D. Lee, C. Wei, D.I. Pineda, R.M. Spearrin, *J. Quant. Spectrosc. Radiat. Transf.* **239**, 106636 (2019)
 13. F. Niro, C. Boulet, J.-M. Hartmann, *J. Quant. Spectrosc. Radiat. Transf.* **88**, 483–498 (2004)
 14. R. Rodrigues, C. Boulet, L. Bonamy, J.M. Hartmann, *J. Chem. Phys.* **109**, 3037–3047 (1998)
 15. J.M. Hartmann, L. Rosenmann, M.Y. Perrin, J. Taine, *Appl. Opt.* **27**, 3063–3065 (1988)
 16. J. Boisssoles, C. Boulet, D. Robert, S. Green, *J. Chem. Phys.* **90**, 5392–5398 (1989)
 17. M.L. Koszykowski, L.A. Rahn, R.E. Palmer, M.E. Coltrin, *J. Phys. Chem.* **91**, 41–46 (1987)
 18. J.O. Hirschfelder, C.F. Curtiss, R.B. Bird, *Molecular Theory of Gases and Liquids*, 2nd edn. (Wiley, New York, 1964)
 19. A. Ben-Reuven, *Phys. Rev.* **145**, 7–22 (1966)
 20. G.B. Rieker, J.B. Jeffries, R.K. Hanson, *Appl. Opt.* **48**, 5546–5560 (2009)
 21. H. Li, G.B. Rieker, X. Liu, J.B. Jeffries, R.K. Hanson, *Appl. Opt.* **45**, 1052–1061 (2006)
 22. K. Sun, X. Chao, R. Sur, C.S. Goldenstein, J.B. Jeffries, R.K. Hanson, *Meas. Sci. Technol.* **24**, 125203 (2013)
 23. R.M. Spearrin, C.S. Goldenstein, J.B. Jeffries, R.K. Hanson, *Appl. Opt.* **53**, 1938–1946 (2014)
 24. R.M. Spearrin, W. Ren, J.B. Jeffries, R.K. Hanson, *Appl. Phys. B Lasers Opt.* **116**, 855–865 (2014)
 25. L.H. Ma, L.Y. Lau, W. Ren, *Appl. Phys. B Lasers Opt.* **123**, 1–9 (2017)
 26. K.-P. Cheong, L. Ma, Z. Wang, W. Ren, *Appl. Spectrosc.* **73**, 529–539 (2019)
 27. J.M. Kriesel, N. Gat, B.E. Bernacki, R.L. Erikson, B.D. Cannon, T.L. Myers, C.M. Bledt, J.A. Harrington, Hollow core fiber optics for mid-wave and long-wave infrared spectroscopy, in *Proceedings of SPIE—The International Society for Optical Engineering* (2011)
 28. R.M. Spearrin, C.S. Goldenstein, I.A. Schultz, J.B. Jeffries, R.K. Hanson, *Appl. Phys. B* **117**, 689–698 (2014)
 29. E.B. Coy, A method for eliminating beam steering error for the modulated absorption-emission thermometry technique, in *53rd AIAA Aerospace Sciences Meeting* (2015)
 30. L.S. Rothman, I.E. Gordon, R.J. Barber, H. Dothe, R.R. Gamache, A. Goldman, V.I. Perevalov, S.A. Tashkun, J. Tennyson, *J. Quant. Spectrosc. Radiat. Transf.* **111**, 2139–2150 (2010)
 31. J.M. Hartmann, C. Boulet, D. Robert, *Collisional Effects on Molecular Spectra* (Elsevier, New York, 2008)
 32. B.J. McBride, S. Gordon, *Computer Program for Calculation of Complex Chemical Equilibrium Compositions and Applications* (NASA, Cleveland, 1996)
 33. D. Romanini, K.K. Lehmann, *J. Chem. Phys.* **105**, 81–88 (1996)
 34. A.S. Pine, J.P. Looney, *J. Chem. Phys.* **96**, 1704–1714 (1992)
 35. J.P. Looney, G.J. Rosasco, L.A. Rahn, W.S. Hurst, J.W. Hahn, *Chem. Phys. Lett.* **161**, 232–238 (1989)
 36. T. Dreier, G. Schiff, A.A. Suvernev, *J. Chem. Phys.* **100**, 6275–6289 (1994)
 37. J. Bonamy, L. Bonamy, D. Robert, M.L. Gonze, G. Millot, B. Lavorel, H. Berger, *J. Chem. Phys.* **94**, 6584–6589 (1991)
 38. F. Beyrau, A. Datta, T. Seeger, A. Leipertz, *J. Raman Spectrosc.* **33**, 919–924 (2002)

Publisher's Note Springer Nature remains neutral with regard to jurisdictional claims in published maps and institutional affiliations.